

DETERMINING OPTICAL CONSTANTS OF URANIUM
NITRIDE THIN FILMS IN THE EXTREME
ULTRAVIOLET (1.6-35 NM)

by

Marie K. Urry

Submitted to the Department of Physics and Astronomy in partial fulfillment
of graduation requirements for the degree of
Bachelor of Science

Brigham Young University

December 2003

Advisor: R. Steven Turley

Thesis Coordinator: Justin Peatross

Signature: _____

Signature: _____

Department Chair: Scott D. Sommerfeldt

Signature: _____

Abstract

I discuss deposition and characterization of reactively-sputtered uranium nitride thin films. I also report optical constants for UN at 13 and 14 nm and reflectance over the range 1.6-35 nm. Measured reflectance over that range is much lower than calculated, possibly due to an unpredicted film density, and UN is shown to oxidize more readily than expected.

Acknowledgments

I am in awe at the wonderful people I have been blessed to work with in this project. My research advisers Drs. Turley and Allred have been absolutely indispensable in their kind teaching and advice. Thanks to John Ellsworth and Elke Jackson for personal instruction and for help with the Monarch. Thanks to Jennie Guzman, Niki Farnsworth, and Liz Strein who have put in many hours on this project and have been good friends. Important assistance was also provided by Kristi Adamson, Luke Bissell, Mindy Tonks, and Winston Larsen. I am grateful for the undergraduate research program at BYU and the experience it has afforded me. Greatest thanks to my parents for helping me get here and for their continuing support and encouragement in all of my endeavors and to my grandparents for a life-long love of learning.

List of Figures	vi
List of Tables	viii
1 Introduction	1
1.1 Application	1
1.2 Optical Constants	2
1.3 Project Focus	7
2 Uranium Nitride Thin Films	8
2.1 Sputtering	8
2.2 Characterization	11
2.2.1 X-ray Photoelectron Spectroscopy	11
2.2.2 X-ray Diffraction	13
2.2.3 Ellipsometry	17
2.2.4 Atomic Force Microscopy	19
2.2.5 Transmissin Electron Microscopy	21
3 Reflectance Data	22
3.1 Advanced Light Source	22
3.2 Data	23
4 Conclusions and Results	27
A Appendix: Monochromator and Reflectometer	30
A.1 Function	30
A.2 Improvements	33
B Appendix: Standard Operating Procedures	38
B.1 Bringing the Monochromator and O-chamber to Vacuum	38
B.2 Shutting Down for the Night	39
B.3 Igniting the Light Source	40

B.4	Turning on the Detector	41
B.5	How to Use Stagecontrol	42
B.6	How to Use Channeltron	43
B.7	Stage Alignment	44
B.8	How to Use VAR (Testing a Sample)	46
B.9	Venting the System (Bringing it to Atmosphere)	47
B.10	How to Change a Sample	48
B.11	Aligning the Grating Rulings	48
B.12	Optical Alignment	49
B.13	Aligning the Pinhole	50

List of Figures

1.1	Delta vs. beta plot for several materials at 5.6 nm	4
1.2	Reflectance of Au, Ni, and U computed using CXRO	5
1.3	Reflectance of U, UO ₂ , and UN computed using CXRO	6
2.1	Sputtering chamber cross-section	8
2.2	N ₂ partial pressure when sputtering vs. N/U ratio	9
2.3	Geometry of sputtering system	10
2.4	XPS concept diagram	11
2.5	XPS scan of sample UN003	12
2.6	XPS scan of sample UN004	12
2.7	Magnification of Figure 2.6	12
2.8	Magnification of Figure 2.7	12
2.9	XRD run for sample UN004	14
2.10	XRD run for sample UN003	14
2.11	Change in theta for 4 peaks versus thickness from IMD	15
2.12	XRD fit and data	16
2.13	Change in thickness vs. time as measured by XRD	17
2.14	AFM schematic	19
2.15	Plot of AFM data showing relationship of RMS to length scale	20
2.16	Image produced by TEM	21
3.1	ALS schematic	22
3.2	Stages in ALS reflectometer	22
3.3	ALS and CXRO reflectance at 5 degrees	24
3.4	ALS and CXRO reflectance at 10 degrees	24

3.5	ALS and CXRO reflectance at 15 degrees	25
4.1	CXRO data with corrected density and RMS and ALS measurements	28
A.1	Monochromator and reflectometer layout	30
A.2	Hollow cathode light source	31
A.3	Reflectometer schematic	32
A.4	Spot of leak in light source gas line	34
A.5	Saddle point in beam profile	36
A.6	Full-width half-max approach to finding beam center	36
B.1	Monochromator roughing pump	51
B.2	Above the monochromator	51
B.3	O-chamber exterior	51
B.4	Beneath the o-chamber	51
B.5	O-chamber roughing pump	51
B.6	Hollow cathode light source	52
B.7	Gas tanks and water lines	52
B.8	Water lines	52
B.9	Voltage source	52
B.10	O-chamber interior	53
B.11	Wavelength counter	53
B.12	Schematic for aligning grating	53
B.13	Schematic for monochromator and o-chamber interior	53

List of Tables

2.1	XPS identifying energy peaks	11
2.2	TEM and literature lattice structure sizes	21
3.1	δ and β calculated for UN	26
3.2	Comparison of calculated δ and β and Lunt's results for UO	26

Chapter 1

Introduction

The extreme ultraviolet (EUV) region, defined as 10-100 nm, is currently gaining importance. Thin film mirrors, so called because they are less than 1 μm thick, are a form of optics important for utilizing EUV light. There is still much to be learned about optical constants in this region for many important compounds that could be used for thin film mirrors. No previous studies have been found of the optical properties of uranium nitride films, which are the specific topic of this paper, despite their having higher theoretical reflectivity than the mirrors currently used in the EUV.

1.1 Application

The EUV region has potential for many applications in industry and research. For example, much can be learned by studying EUV emissions of terrestrial objects. In March of 2000 the IMAGE (Imager for Magnetopause-to-Aurora Global Exploration) Satellite was launched carrying three multilayer mirrors made by the XUV optics group at Brigham Young University. These mirrors have been used for imaging the magnetosphere of the earth [1]. Astronomers are also interested in using this energy band for other purposes, including studying the cosmic background of the universe [2].

EUV light also has applications in lithography. Current projection photolithography techniques are incapable of making computer chips much smaller than they already do because of diffraction. Diffraction limits the area light can be focused to no smaller than one half of the wavelength [3]. Because wavelengths in the EUV are incredibly short, they can be focused to a smaller area and thus be used to make smaller

chips. It is estimated that this new technology, called EUV lithography, will be used in production by 2009 [4].

Because these wavelengths in the EUV are so short, they could also be used in the medical and biological fields to image smaller features in cells. Diffraction requires the wavelength of the light used to be smaller than the object being viewed, so short wavelengths must be used to view tiny objects. Unfortunately, water is opaque at most shorter wavelengths, so current techniques require that a sample be dried and stained. However, because water is reasonably transparent and carbon is opaque for the range 23.4-43.8 Angstroms, wet slides could be used for this range. Unlike current techniques, EUV light would allow cells to be viewed in nearly their natural environment [5].

1.2 Optical Constants

In order to utilize EUV light applications, it is necessary to have an understanding of the optical properties of the materials used for optical instrumentation in the energy band of interest. Having a good idea of the optical constants of a material allows calculation of the reflectance and transmission expected when using that material. Reflectance is calculated by dividing the intensity reflected from a film, I_f , by the intensity incident on the film, I_0 :

$$R = \frac{I_f}{I_0}. \quad (1.1)$$

A main goal of this thesis is the index of refraction, generally written

$$\mathcal{N} = n + i\kappa, \quad (1.2)$$

where n is the real part of the index of refraction and κ the imaginary part, is called the coefficient of absorption. When discussing the EUV, a slight variation of this is used. In

the EUV n is very near that of vacuum, 1, in almost all media, so it is written $n=1-\delta$ and δ is specified rather than n . Also β is used instead of κ as the coefficient of absorption.

When \mathcal{N} is known, reflectance from multiple layers can be computed using the Parratt formula and the Fresnel coefficients [6] [7]. The Fresnel coefficients are given for the s- and p-polarizations of light as follows:

$$f_{p,m} = \frac{\mathcal{N}_{m-1}^2 q_m - \mathcal{N}_m^2 q_{m-1}}{\mathcal{N}_{m-1}^2 q_m + \mathcal{N}_m^2 q_{m-1}} \quad \text{and} \quad f_{s,m} = \frac{q_m - q_{m-1}}{q_m + q_{m-1}} \quad (1.3)(1.4)$$

where m is the m th surface in the mirror and

$$q_m = \sqrt{\mathcal{N}_m^2 - \cos^2 \theta_i}. \quad (1.5)$$

Here θ_i is the angle from grazing of the light incident on the film. Now the recursive Parratt formula can be used:

$$r_{s,m} = C_m^4 \frac{f_{s,m} + r_{s,m-1}}{1 + f_{s,m} r_{s,m-1}} \quad \text{and} \quad r_{p,m} = C_m^4 \frac{f_{p,m} + r_{p,m-1}}{1 + f_{p,m} r_{p,m-1}}, \quad (1.6)(1.7)$$

where

$$C_m = e^{iq_m D_m \pi / \lambda}. \quad (1.8)$$

Finally, reflection from the film is given using the coefficients for the M th layer:

$$R_s = |r_{s,M}|^2 \quad \text{and} \quad R_p = |r_{p,M}|^2. \quad (1.9)(1.10)$$

For a single, thick layer in a vacuum, reflection is proportional to $\delta^2 + \beta^2$, assuming δ and β are much less than one and θ is near normal. For maximum reflection a large δ and large β are desired, making the optical constants as different from those of vacuum as possible. $x^2 + y^2$ is the equation for a circle, so the materials producing equally large reflections lie in a circle on the δ vs. β plot (Figure 1.1). (Notice on the given plot that

the δ scale goes up to .03 while the β scale only goes to .018, so the circle is elongated vertically.) It is advantageous to sacrifice a large β in order to get a larger δ because, for thicker, multilayer films, a large β means large absorption, resulting in a lower reflection.

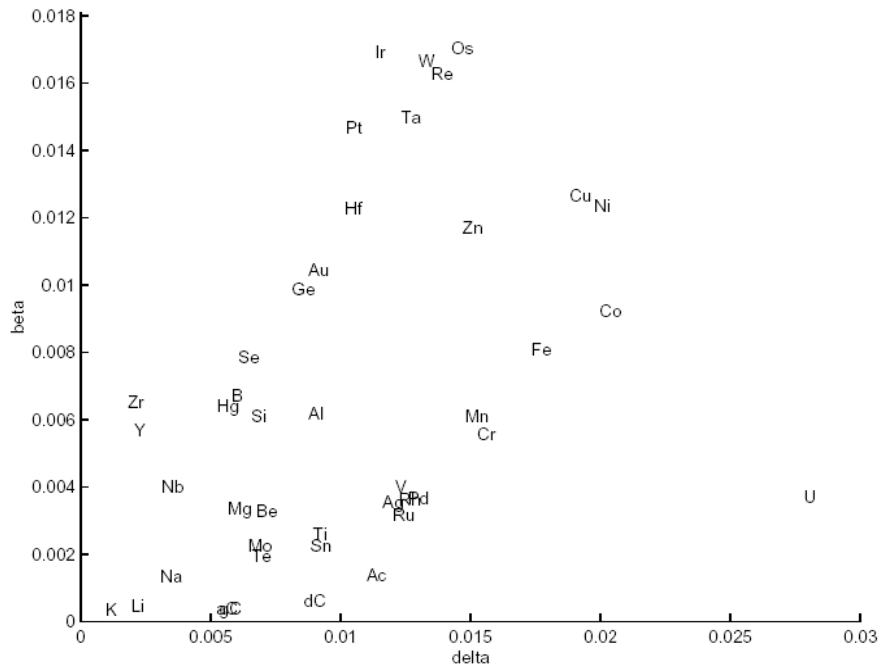


Figure 1.1: Delta vs. beta plot for several elements at 5.6 nm [1]

As a result of the relatively large δ in the EUV, uranium has a very high theoretical reflectance in this region. Figure 1.2 shows reflectance, computed from the CXRO website [8], for gold and nickel, the two most common mirrors used in the EUV, and for uranium, emphasizing the reasons for studying uranium.

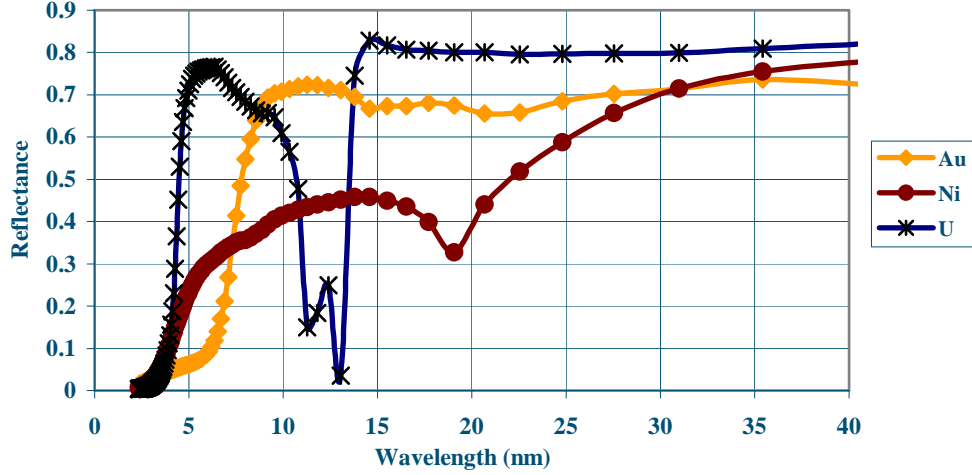


Figure 1.2: Reflectance of gold, nickel, and uranium at 10 degrees from grazing computed using CXRO

Another convenient way to discuss reflection is in terms of the atomic scattering factor f . f is written

$$f = f_1 + i f_2, \quad (1.11)$$

where f_1 and f_2 are given by δ and β as follows [9]:

$$\delta = \frac{n_a r_e \lambda^2}{2\pi} f_1 \quad (1.12)$$

$$\beta = \frac{n_a r_e \lambda^2}{2\pi} f_2. \quad (1.13)$$

n_a is the atomic density, r_e is classical electron radius, and λ is wavelength of the light in the material. The atomic scattering factor is also related to the number of free electrons, so the number of effectively free electrons in a material can be used to approximate the expected reflectance.

Unfortunately, uranium readily oxidizes in air, leaving fewer effectively free electrons and reducing the reflectance, so uranium is not a reasonable option for optics on

its own. It is anticipated that uranium nitride is less chemically active but will have a comparable reflectance (Figure 1.3).

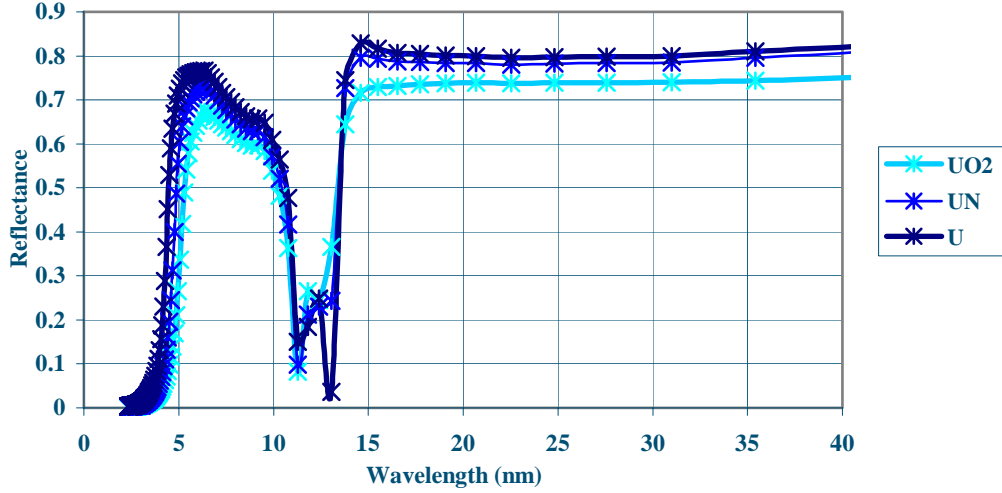


Figure 1.3: Reflectance of U, UO₂, and UN at 10 degrees from grazing as computed using CXRO

The CXRO data is computed using the atomic scattering factors of uranium and nitrogen. The scattering factors of the two materials are combined by weighting them according to their respective densities in the film. This speculative approach works well for shorter wavelengths, but it begins to break down for the EUV, so these calculations are simply best guesses.

In determining optical constants, it is also useful to write them in terms of the dielectric constant [9]:

$$\mathcal{N}^2 = \varepsilon = \varepsilon_1 + i\varepsilon_2, \quad (1.14)$$

where

$$\varepsilon_1 = (1 - \delta)^2 - \beta^2 \quad (1.15)$$

$$\varepsilon_2 = 2(1 - \delta)\beta. \quad (1.16)$$

The dielectric is also the proportionality constant between electric field, \mathbf{E} , and electric displacement, \mathbf{D} :

$$\mathbf{D}(\mathbf{x}, \omega) = \varepsilon(\omega)\mathbf{E}(\mathbf{x}, \omega) \quad [10]. \quad (1.17)$$

This will be convenient in applications that allow the dielectric constant to be more easily calculated than the optical constants.

1.3 Project Focus

The focus of this project was to make and experimentally determine the indices of refraction of thin-film UN from 1.6 to 35 nm. Chapter 2 addresses creating the films and studying their composition and depth. Chapter 3 discusses obtaining reflectance data and the last chapter addresses resulting optical constants, conclusions, and possible future research.

Chapter 2

Uranium Nitride Thin Films

2.1 Sputtering

To study the optical constants of uranium nitride thin films, the thin films must first be deposited. Our films are sputtered using RF (radio frequency) magnetron sputtering (Figure 2.1). In this process, a plasma of argon is created in the center of the sputtering chamber using a radio frequency voltage. The plasma is localized above the target using a magnetic field. This allows sputtering to be done at a lower pressure, increasing the deposition rate. An electric field is present such that the ionized argon is accelerated toward a uranium target located at the bottom of the chamber. Argon is a heavy atom so, once accelerated, it has sufficient kinetic energy to knock uranium atoms free from the target. The resulting release of uranium atoms from the target is the specific process referred to as sputtering. The interest for this work is the subsequent deposition of uranium throughout the system and specifically on substrates suspended from the top of the chamber.

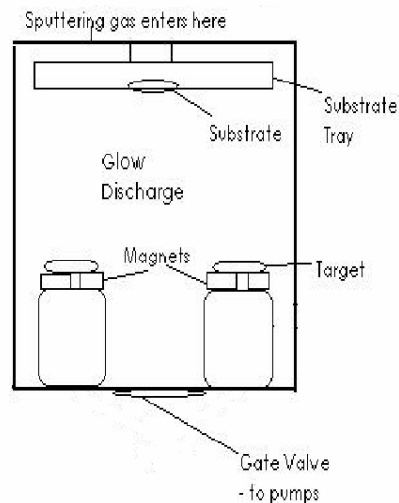


Figure 2. 1: Sputtering chamber cross-section [2]

Uranium nitride was deposited on several different substrates simultaneously so that the films created may be studied using many different characterization techniques. To date, only the silicon wafers and carbon coated TEM (Tunneling electron microscopy) grids have now been studied. The deposited films ranged from 10-40 nm in thickness.

By sputtering at low pressures, the mean free path of the particles is increased. We ran at a base pressure between 1 and 15 mtorr, increasing the mean path length to as much as 3 centimeters, a factor of 750,000 more than at atmosphere. Increasing the path length also increases the kinetic energy of the uranium atoms just before they are deposited, leading to films that are smoother, denser, and lower stress. The result is fewer irregularities and fractures in the films.

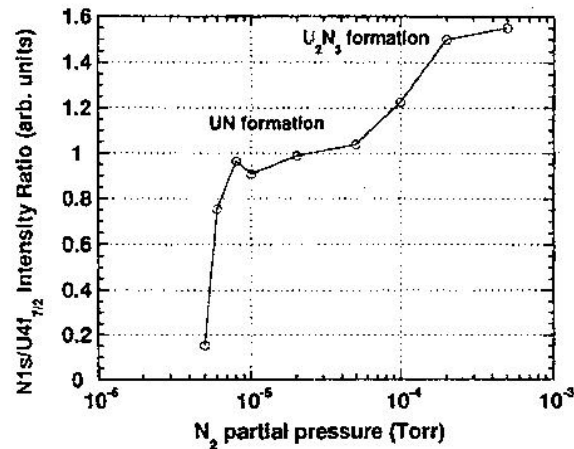


Figure 2.2: N₂ partial pressure when sputtering vs. N/U ratio [11]

Introducing nitrogen to the system during sputtering creates UN_x. The ratio of uranium to nitrogen in the film created is dependent on the nitrogen partial pressure present when the film is sputtered. Figure 2.2 shows that a nitrogen partial pressure of less than 10⁻⁴ torr is needed to create the desired uranium mononitride. When the first two samples were sputtered (UN002 and UN003), the system was not designed for

control of the nitrogen pressure in this range. Some change in plumbing of the system allowed more accurate control. The last two samples (UN004 and UN005) were sputtered at a nitrogen partial pressure of about 10^{-5} torr. Section 2.2 discusses characterization of the films to ensure that they are indeed the stoichiometry expected.

The thicknesses deposited on the substrates are measured indirectly by a quartz crystal thickness monitor. Because the monitor is located slightly to the side of the substrates, it does not receive the same amount of deposition as the substrates (Figure 2.3). There may be less deposition on the monitor because of the geometry. There may also be an offset if the shutter covers the substrates better than it does the monitor. The shutter is used to cover the sample to sputter the uranium target without depositing on our samples. This is done especially for cleaning off oxides and other dust or residues that build up on the target while exposed to atmosphere.

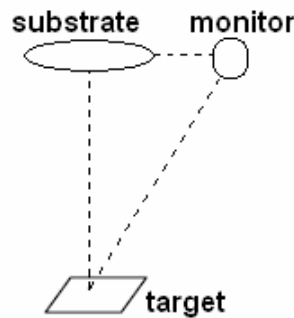


Figure 2.3: Geometry of sputtering system

When well-calibrated, this geometric offset can be corrected mathematically. Our system, however, has not yet been calibrated for such a correction and the result is a poorly defined thickness. More accurate measurements of thickness will be addressed in the next section.

2.2 Characterization

After samples have been made, questions still remain. It is necessary to learn more about their composition, thickness, and roughness before measuring optical constants. Different characterization techniques used to study the films will now be discussed. It is important to understand how all of these techniques work in order to obtain and interpret data.

2.2.1 X-ray Photoelectron Spectroscopy

X-ray photoelectron spectroscopy (XPS) uses the photoelectric effect to study film composition. An x-ray beam of known energy is shone on the sample (Figure 2.4). The energy from the beam will cause electrons to be released with a kinetic energy equal to the energy of the incident beam minus the binding energy. From measurements of the energy of the released electrons, the binding energy of the atoms on the surface of the film is calculated and hence the chemical composition of the film is known. Table 2.1 lists expected electron energy measurements of interest in this study.

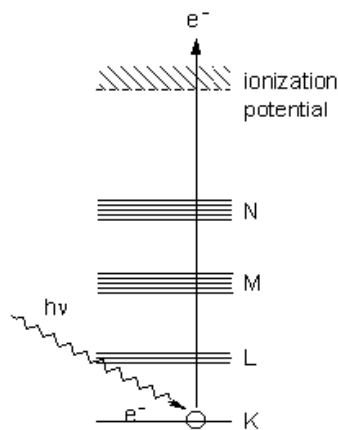


Figure 2.4: XPS concept diagram [12]

Scan of Surface Identifying Peaks:
100eV – U 5d5/2
280eV – C 1s
380eV – U 4f7/2
390eV – U 4f5/2
398eV – N 1s
530eV – O 1s
740eV – U 4d5/2
780eV – U 4d3/2
980eV – Auger O Line

Table 2.1: XPS identifying energy peaks

Figures 2.5-2.8 are XPS graphs of energies of electrons ejected from the surface versus intensity measured in photon counts for samples UN003 and UN004. The first two plots are overall energy scans of the samples. The energy peaks expected are those for uranium and nitrogen. Zooming in on the UN004 plot over the range 370-410 eV (Figure 2.7), lines at 380 and 390 eV for uranium and at 398 eV for nitrogen are expected. The lines for uranium are evident, but, zooming in once more (Figure 2.8), there is only noise where we had hoped to see a nitrogen peak. There is, however, a peak at 530 eV for oxygen. The data is very similar for sample UN003.

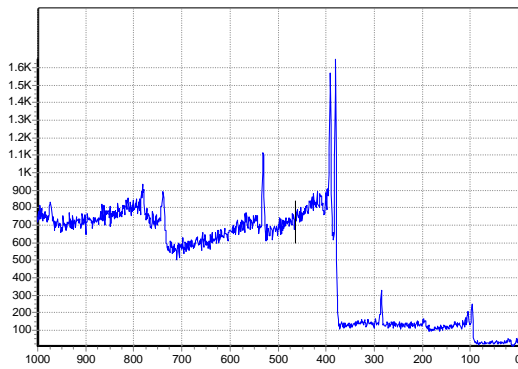


Figure 2.5: XPS scan of sample UN003

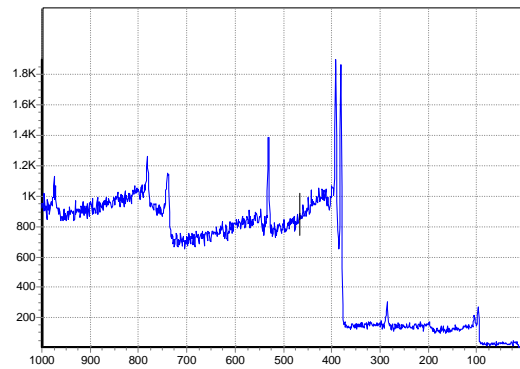


Figure 2.6: XPS scan of sample UN004

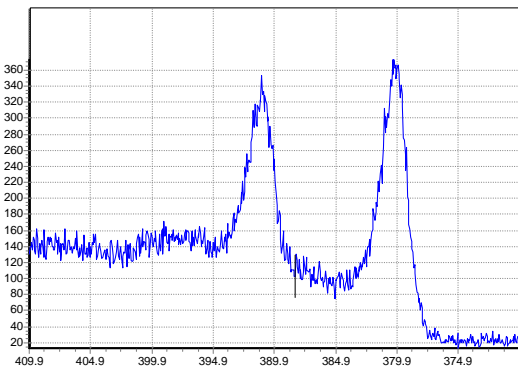


Figure 2.7: Magnification of Figure 2.6

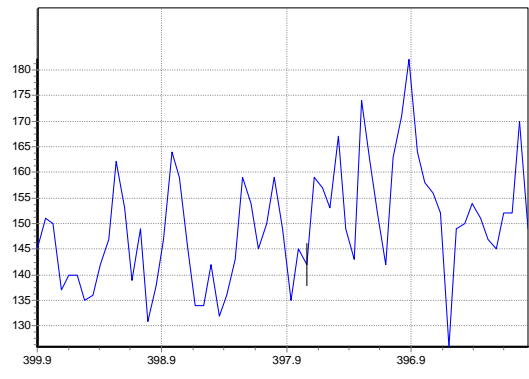


Figure 2.8: Magnification of Figure 2.7

These results show that the surfaces of these samples are UO_2 rather than UN_x . This unexpected composition is most likely due to oxidation of the surface, but it could also be a larger problem with sample composition. This will be further explored in section 2.2.5.

2.2.2 X-ray Diffraction

X-ray diffraction uses a Cu K_α x-ray beam incident on the film. In this case the intensity of the reflected beam is measured as the angle of the incident beam is changed in order to find the thickness of the film. Just as bright patterns are created on a soap bubble because of differences in thickness, different wavelengths of light experience constructive interference for different thicknesses in our films. Here it is impractical to change thickness. Instead we vary the angle of the incident beam at near grazing, thus changing the effective thickness experienced by the light. The maxima in intensity are expected at angles given approximately by the equation for Bragg diffraction from a single layer:

$$m \lambda = 2d \sin \theta, \quad (2.1)$$

where m is an integer, λ is the wavelength of the x-ray inside the film, and d is the thickness of the film. By scanning through θ , we can find maxima at several m to discover the thickness of a film.

The first plot shown here is for sample UN004 (Figure 2.9). The shape of the graph is as expected. Figure 2.10 is from sample UN003. There is a beat pattern evident, suggesting a bilayer. This is most likely due to oxidation of the surface, leaving a layer of UO_2 or UNO_x over a layer of UN_x . It could also be a result of sputtering. If all

of the UO_2 were not removed from the surface of the uranium target before depositing the sample or if the N_2 partial pressure changed during deposition, the stoichiometry of the film could have changed as it was being created.

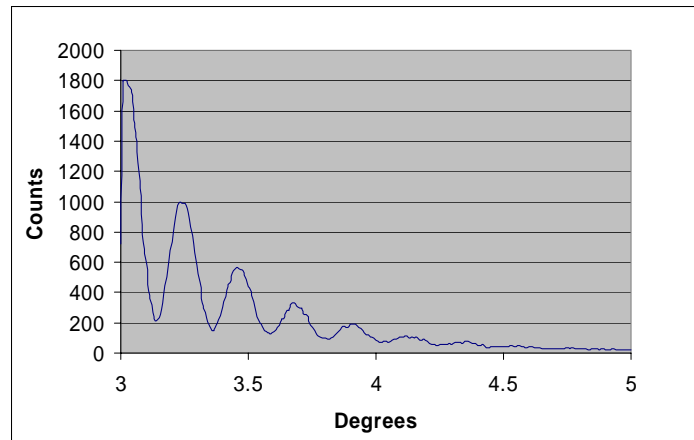


Figure 2.9: XRD run for sample UN004

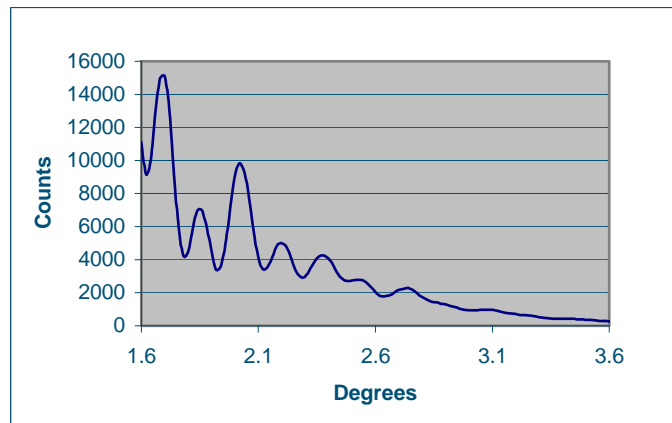


Figure 2.10: XRD run for sample UN003

There are two ways to use XRD data to determine thickness of a sample. One is to compare the data to plots created in IMD, a program by David Windt [13]. IMD generates theoretically, just as XRD does experimentally, a plot of angle versus intensity

for a film of given thickness. To compare the plots, change in theta between four peaks centered at 3 degrees was measured for several IMD plots of different thicknesses. This change in theta is plotted versus thickness in Figure 2.11. The change in theta between four peaks centered at 3 degrees can then be counted on the XRD plots and the thickness of the film learned from comparison to IMD plots.

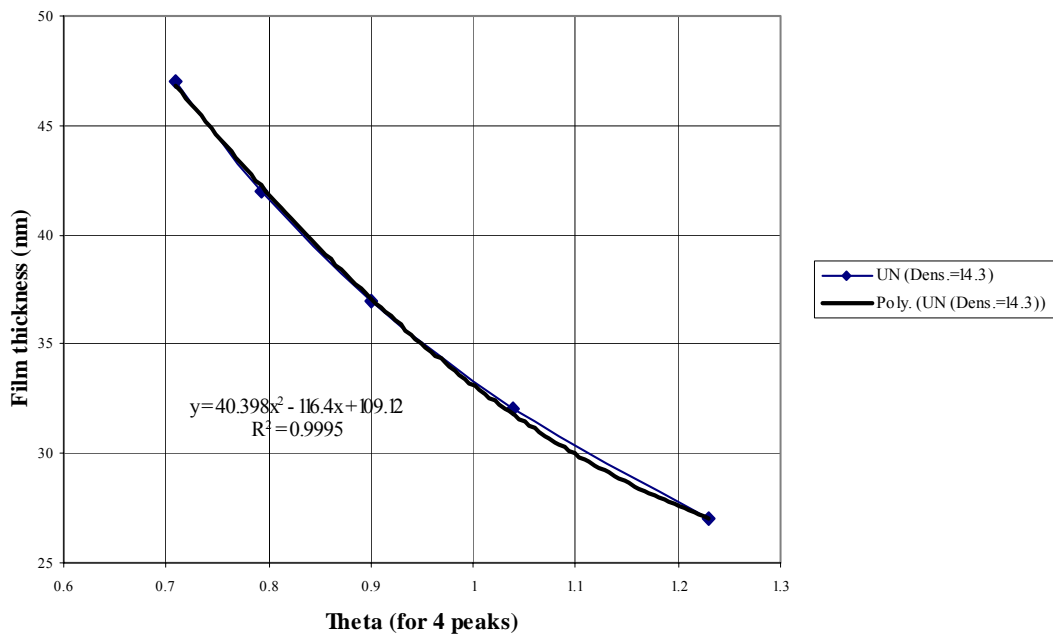


Figure 2.11: Change in theta for 4 peaks centered at 3 degrees vs. thickness from IMD

Another interpretation of XRD data is mathematical modeling. This was done with a program written in Fortran called fitxrd. The fit can be seen in Figure 2.12. The difference in slope is probably due to misalignment of the system, but the peaks match exactly.

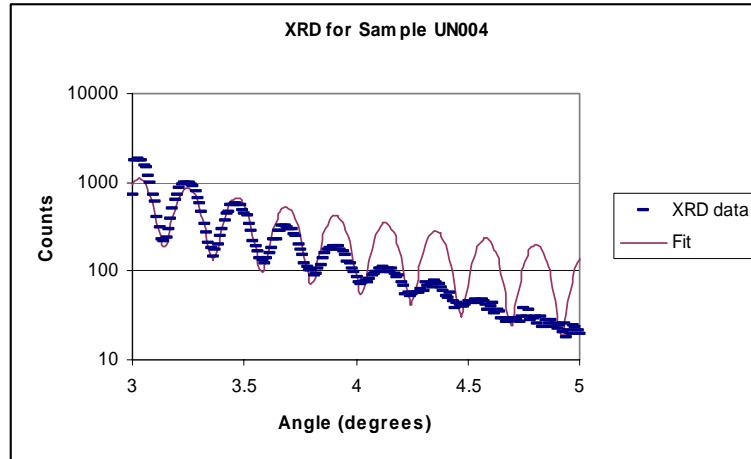


Figure 2.12: XRD fit and data

Using both methods and multiple XRD runs to characterize the film, on 2 October 2003, 26 hours after the film was removed from the sputtering system, the resulting thickness was determined to be 38 nm. This is much larger than the thickness measured by the crystal monitor in the sputtering system, and possibly indicates a density lower than supposed.

Measurements of sample UN004 were taken on several different days, revealing a change in thickness over time (Figure 2.13). After 10 days, the peaks revealed a thickness change of 12%. This oxidation rate is much greater than expected [14]. Thickness changes in time as:

$$thickness = 3.569271 \cdot \ln(0.111438 \cdot time + .839977) + 100 \quad (2.2)$$

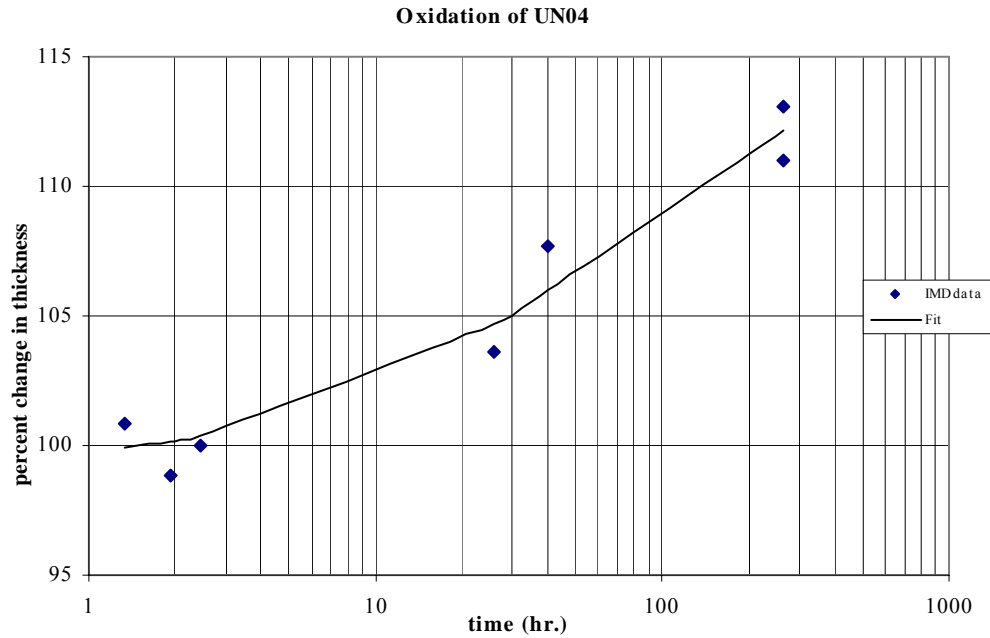


Figure 2.13: Change in thickness vs. time as measured by XRD

2.2.3 Ellipsometry

Ellipsometry uses a visible or UV light reflected at near grazing angles from the surface of a sample to determine indices of refraction or thickness. In ellipsometry, light of a known ratio of s- and p-polarized light is incident the sample. The polarization of the reflected light is measured as the angle of the incident beam is changed. S- and p-polarizations of light are reflected differently. Their relationship is sufficient to learn optical constants or thickness if the film is well characterized and a decent model for the optical constants is defined. A general oscillator model was used for these calculations, modeling the motion of the electrons in an electromagnetic field as springs attached to the nucleus.

Ellipsometry reports values of Ψ and Δ . Ψ is the ratio of intensities of the s- and p-polarizations of the reflected light. Δ is the phase difference or the difference between imaginary parts of s- and p-polarizations of the light. Ψ and Δ are related to r_p and r_s by [2]:

$$\frac{r_p}{r_s} = \tan(\Psi)e^{i\Delta}. \quad (2.3)$$

r_s and r_p are given by equations 1.2 through 1.8.

The Lorentz oscillator model finds ϵ_1 and ϵ_2 using

$$\frac{\epsilon(\omega)}{\epsilon_0} = 1 + \sum_j \frac{Ne^2 f_j}{\epsilon_0 m(\omega_j^2 - \omega^2 - i\omega\gamma_j)} \quad [10]. \quad (2.4)$$

Here N is the number of molecules per unit volume and f_j is the number of electrons with binding energy ω_j and damping constant γ_j per molecule. The general oscillator model is very similar but allows for different types of oscillators at a time. From the dielectric constant, δ and β , and hence n and κ , can be determined (Equations 1.14-16).

Unfortunately, the range of our ellipsometer is 189-1000 nm, outside of the specific range of this paper. Ellipsometry can still be used, however, to check the thickness as previously determined from XRD. If we are able to obtain reasonable optical constants in the range of the ellipsometer assuming the thickness found from XRD, then our previous thickness measurement is reaffirmed.

The results obtained from ellipsometry were nonphysical, with an instantaneous jump in both n and κ . This edge alone does not necessarily disqualify the fit, but the edge moves depending on the range of wavelengths being fit. To make the ellipsometry

data work, the data needs more constraints. This could be done using the quartz slides for transmission measurements to constrain β .

2.2.4 Atomic Force Microscopy

To learn about the roughness of our film, atomic force microscopy (AFM) was used. In this instrument, a tiny tip on the end of a cantilever is dragged across the surface of the film with a force such that the cantilever goes up and down as it passes bumps and valleys in the sample, much as the needle in a record player (Figure 2.14). A laser beam is reflected from the top of the cantilever and deflected at different angles depending on the height of the cantilever. The deflection of the laser is measured using a photodiode detector. From this we learn the roughness of the surface of our film.

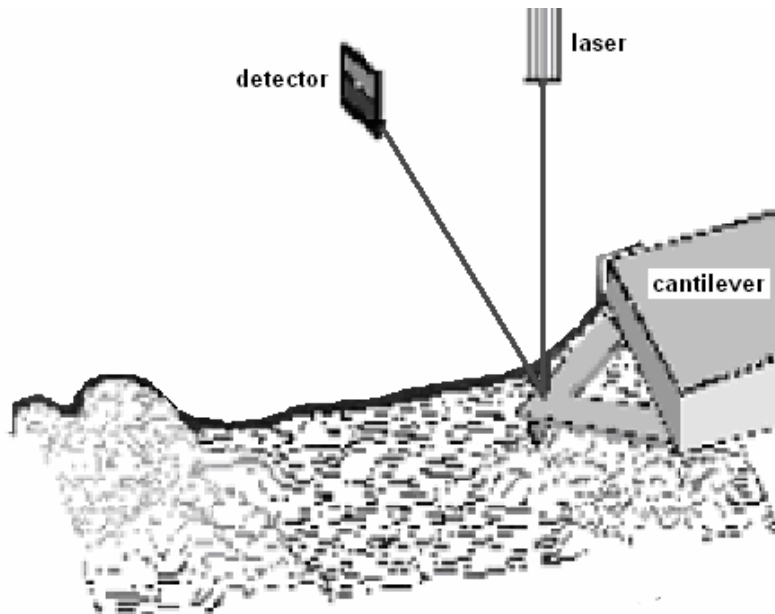


Figure 2.14: AFM schematic [15]

We took measurements at three different spots on sample UN004 over three different length scales. These measurements are presented in Figure 2.15. The tip of the

cantilever is 10 nm in diameter, so we can only measure roughness reliably on a length scale of about 50 nm or larger. Luckily, roughness is generally fractal, or self-similar with the same pattern apparent over different length scales, so we can extrapolate the roughness from the larger, measurable scales down to the scale of interest. The data was plotted in Excel and the resulting equation was:

$$\log\left(\frac{1}{RMS}\right) = -0.5666 \cdot \log(\text{length scale}) + 1.667. \quad (2.5)$$

Here RMS and length scale are given in nanometers. Because roughness affects reflectance, the resulting RMS value can be used in ellipsometry and other reflectance calculations for a more accurate model of our films.

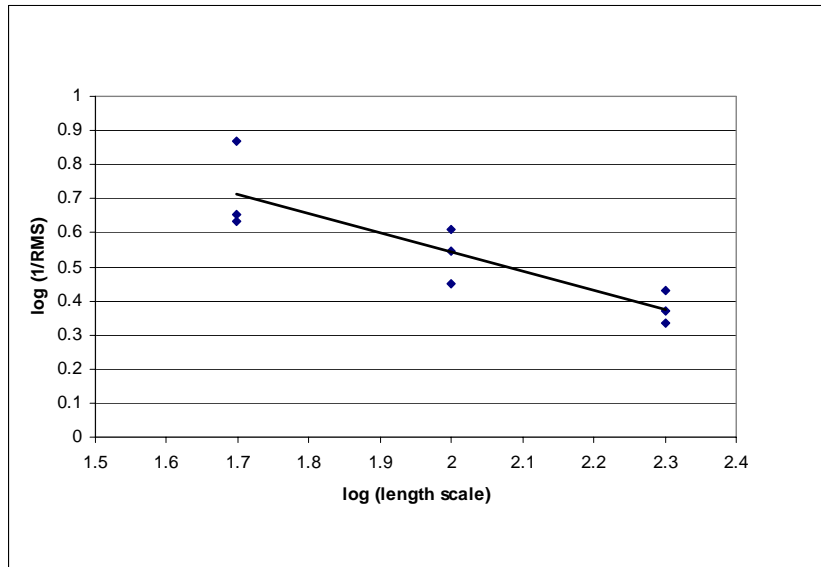


Figure 2.15: Plot shows relationship of RMS (nm) to the length scale (nm)

2.2.5 Transmission Electron Microscopy

In the characterization technique of transmission electron microscopy (TEM), a beam of electrons is transmitted through a film deposited on a TEM grid. The atoms in the sample deflect the electron beam to create a circular pattern (Figure 2.16). The radii of the circles in the pattern are a result of the arrangement and size of the lattice structure in film. These have been the most reliable and helpful data in learning about the composition of our films. See Table 2.2 for the data obtained from TEM. The measured lattice sizes of films UN002 and UN004 show that the samples are indeed U_2N_3 and UN respectively, as expected. The small error could be due to impurities in the films, a difference in bulk material lattice structure reported in literature versus that of thin films, or simply experimental error.

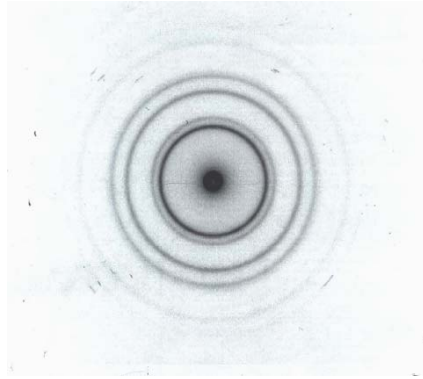


Figure 2.16: Image produced by TEM

SAMPLES	UN002	UN003	UN004
N ₂ Pressure in Sputtering	>1e-4 torr	>1e-4 torr	~1e-5 torr
Suspected Phase	U ₂ N ₃	U ₂ N ₃	UN
Lattice Size			
Literature (Å)	5.34	5.34	4.89
TEM (Å)	5.46		4.98
Ratio (measured/lit)	1.022		1.018

Table 2.2: TEM and literature lattice structure sizes

Chapter 3 Reflectance Data

3.1 Advanced Light Source

The Advanced Light Source (ALS) at Livermore Berkeley National Laboratory is a synchrotron light source. Electrons are accelerated in a circular path by a magnetic field, producing electromagnetic radiation, primarily x-rays. The radiation is directed down beamlines extending from the circular path (Figure 3.1)

At the end of beamline 6.3.2 is a reflectometer. The reflectometer holds a stage for samples and a photodiode detector arranged as shown in Figure 3.2. Scans can be taken varying wavelength with the angle fixed or varying the angle of the stage and the detector with fixed wavelength.

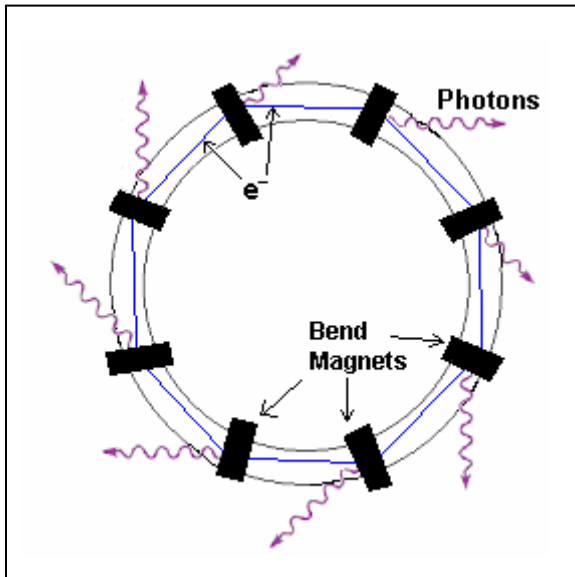


Figure 3.1: ALS schematic [16]

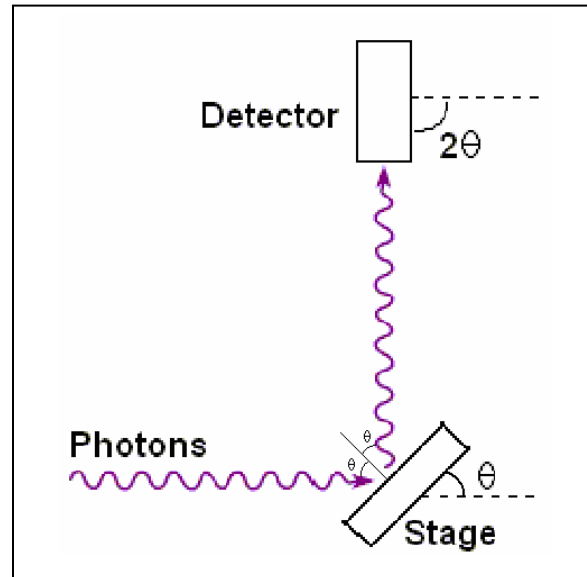


Figure 3.2: Stages in ALS reflectometer

3.2 Data

The wavelength scans of intensity taken at a fixed angle can be converted directly to graphs of wavelength versus reflectance with reflectance given by Equation 1.1. I_0 is measured by moving the film out of the way and measuring the intensity of the undeflected beam. I_f is measured by moving the film to an angle and the detector to twice that angle (see Figure 3.2). Reflection will be a function of the film's angle.

These experimental plots can then be compared to plots created using data from the CXRO website from the Berkeley National Laboratory [8]. No optical constants have been previously measured for uranium nitride, but the CXRO website computes them theoretically as described in Section 1.2.

The ALS beam is 90% s-polarized and 10% p-polarized. These CXRO plots were made accordingly. Figures 3.3-5 show the ALS results and CXRO plots. The large dips in the reflectance data are a result of absorption edges. If an incident photon has energy barely above the binding energy of an electron in the atom, instead of being reflected or transmitted the photon is absorbed and the atom is ionized. This causes a sudden jump in the absorptive coefficient and is manifest in absorption edges. The discrepancy between the theoretical and experimental graphs could be due to oxidation of the sample, roughness, a problem with the ALS data, or an improper assumption about density or in combining atomic scattering factors. Oxidation could be solved in the future by making the sample nearer to the time of the ALS run and keeping the sample in an inert environment. Roughness can be added into the CXRO model and density could also be better studied and added to the model. Another ALS run might also help resolve any

problems with alignment in the earlier runs. Problems with CXRO assumptions have already been discussed (section 1.2).

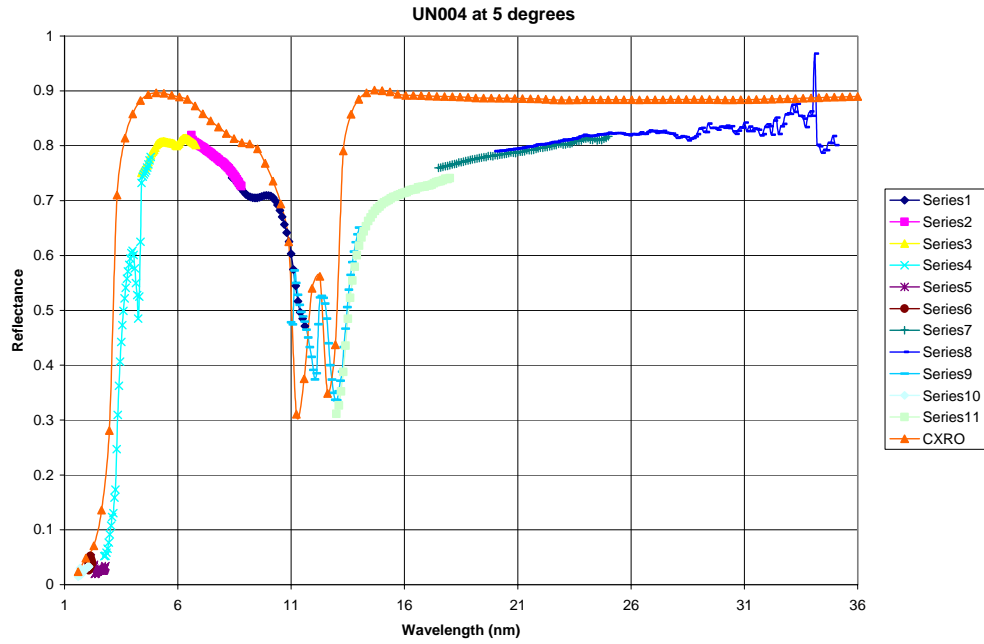


Figure 3.3: ALS and CXRO reflectance at 5 degrees

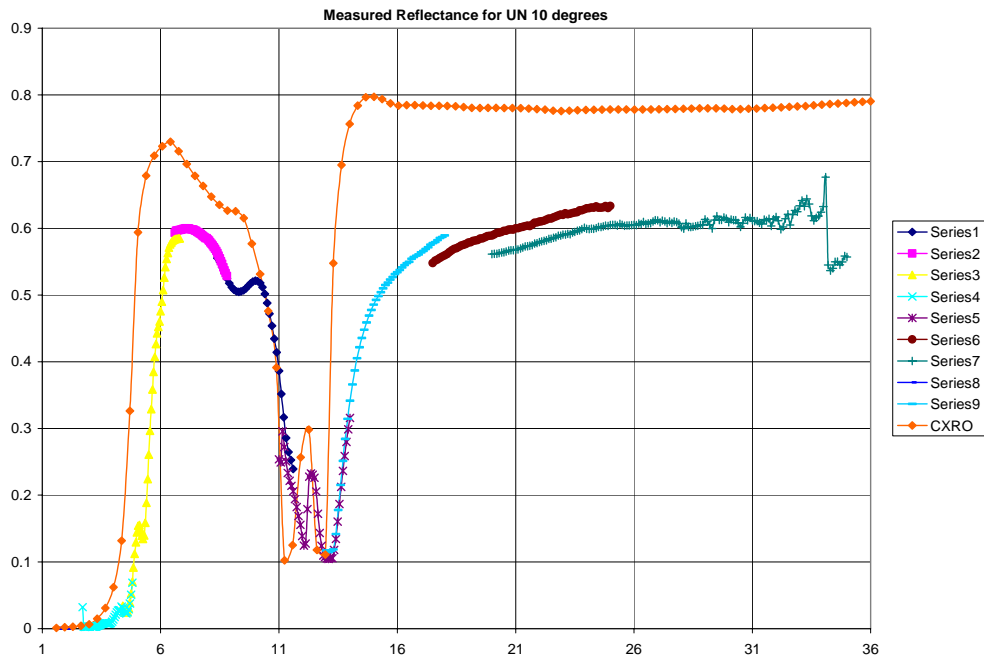


Figure 3.4: ALS and CXRO reflectance at 10 degrees

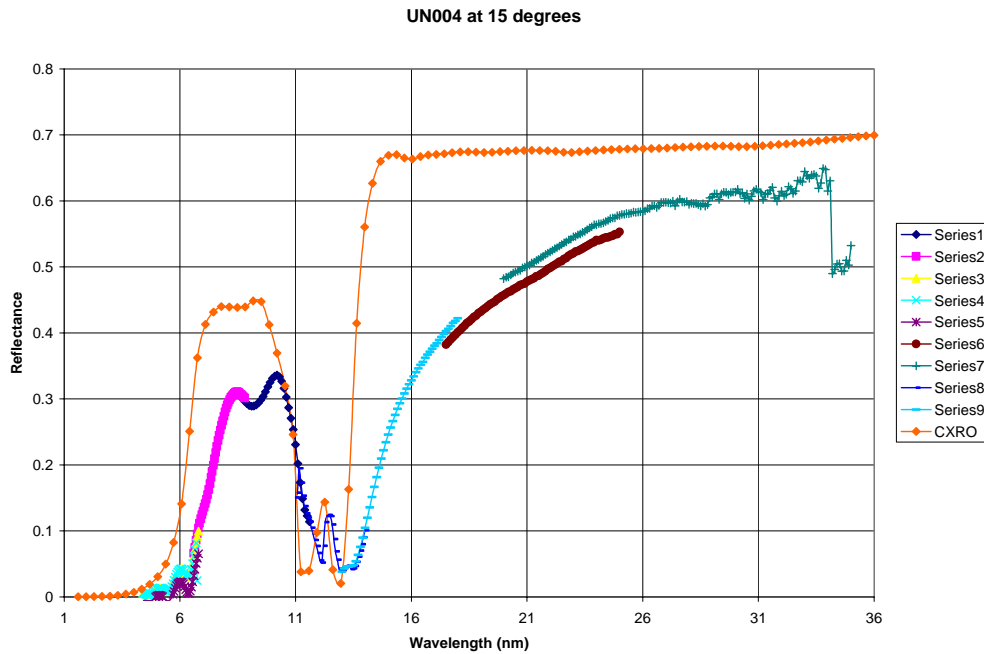


Figure 3.5: ALS and CXRO reflectance at 15 degrees

The angle scans of intensity can be used to calculate the optical constants δ and β , or n and κ . This fitting can be done with a program called fitals. Fitals uses reflectance measurements and equations 1.3-1.10 to calculate n and κ and thickness of the film. Because the intensity dies exponentially with increasing angle but the data at large angles are less affected by alignment, and so more accurate, an updated version of the program, relals, was made. Relals weights the data so that large angle data is fit as accurately as the small angle data even though at large angles the intensity and change in intensity is much less.

Unfortunately only two useful angle scans were taken at the ALS, one at 13 nm and one at 14 nm. These two wavelengths were chosen because they lie on opposite sides of an absorption edge (see Figure 1.3). Frequently, preferred mirrors reflect a given

wavelength of light, say 14 nm, but absorb surrounding wavelengths, say 13 nm, thus cutting out noise for a monochromatic study. The relals data is displayed in Tables 3.1 and 3.2 and discussed in the conclusion.

	δ	β
13 nm	.01152	.0595
14 nm	.0138	.0416

Table 3.1: δ and β calculated for UN

	δ			β		
	Measured	Shannon's Measured	Shannon's Calculated	Measured	Shannon's Measured	Shannon's Calculated
12.5 nm		-.0038	.0057		.0129	.0399
13 nm	-.0228			.0292		
14 nm	.0252	.0229	.0509	.0261	.0103	.0170

Table 3.2: Comparison of calculated δ and β and Lunt's results for UO [2]

Chapter 4

Conclusions and Results

Using several characterization techniques, much was learned about UN. We found that it must be sputtered at a nitrogen partial pressure less than 10^{-4} torr. Sample UN004 was used to study the reflectivity of UN from 1.6 to 35 nm and to find n and k at 13 and 14 nm. We also saw that sample UN004 oxidized much faster than expected.

XRD showed our sample to be 38 nm thick. Fitting ALS data gave a UN thickness of 30.2 nm with an oxide layer of 4.3 nm, for a total thickness of 35.5 nm. Two possible reasons for this small discrepancy are: 1) misalignment of either system or 2) error in the fits. The XRD fit could also be made more accurate by fitting for two layers as was done with the ALS data. Both of these thicknesses are more than the 300 nm predicted by the crystal monitor in the sputtering chamber, suggesting that the films are less dense than the 14.32 g/cm^3 reported in literature [11]. Another measurement of thickness could be taken with the ellipsometer if transmission measurements were taken.

The ALS runs revealed a reflectance much lower than predicted by CXRO, although the shape is near the same, exhibiting predicted absorption peaks. Much of the difference may be accounted for using lower UN density and including RMS roughness in the CXRO calculations (Figure 4.1). As films are deposited, molecules stick wherever they touch the film. As one spot gets hit by molecules and begins to grow, the increased surface area makes it more likely to be hit by more molecules in the future and to continue to grow more quickly than other spots, resulting in non-uniform films of lower density. The oxide layer on the surface and impurities in the film would also have affected reflectance.

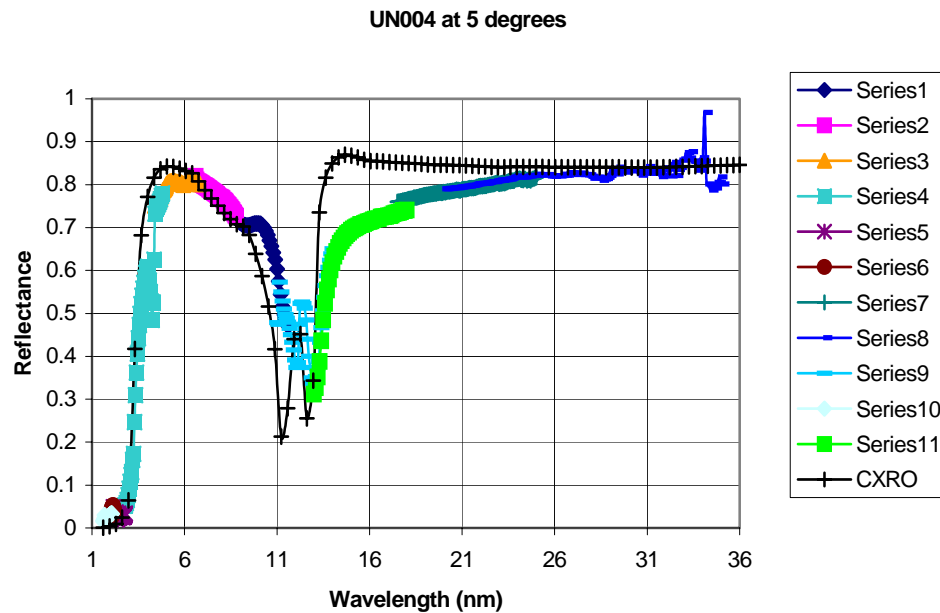


Figure 4.1: CXRO data with density of 10 g/cm^3 and RMS of 2.5 nm and ALS measurements

The measured values of δ and β for UN are similar at 13 and 14 nm and do not show the expected absorption peak between the two (Tables 3.1). This is probably because the two measurements are on opposite sides of a peak in the index of refraction. The fit for the oxide layer, however, does reveal the peak and δ is near that measured by Shannon Lunt for her thesis [2].

Uranium nitride is not as stable as expected in atmosphere and so is not fit as a top layer for a mirror. This was seen using XRD to find a change in thickness of 12% in 10 days. XPS also showed that the surface of the UN film had become UO_x . The oxidation rate could be further studied using XPS depth profiling once the sputterer on the XPS system is fixed, and using more XRD and TEM measurements in time. It would also be useful to take measurements nearer the time of the ALS runs so that thickness and composition are found directly rather than extrapolated from older measurements.

While only one film was studied in depth, these results show that UN of the density created does not exhibit the desired advantages of high reflectivity and low oxidation.

Appendix A Monochromator and Reflectometer

A.1 Function

Our group has a reflectometer for determining optical constants in the range of 30-300 nm (Figure A.1). Maintenance of the reflectometer and accompanying monochromator was primarily my responsibility from May 2003-January 2004 after being trained by Elke Jackson in the winter semester of 2003.

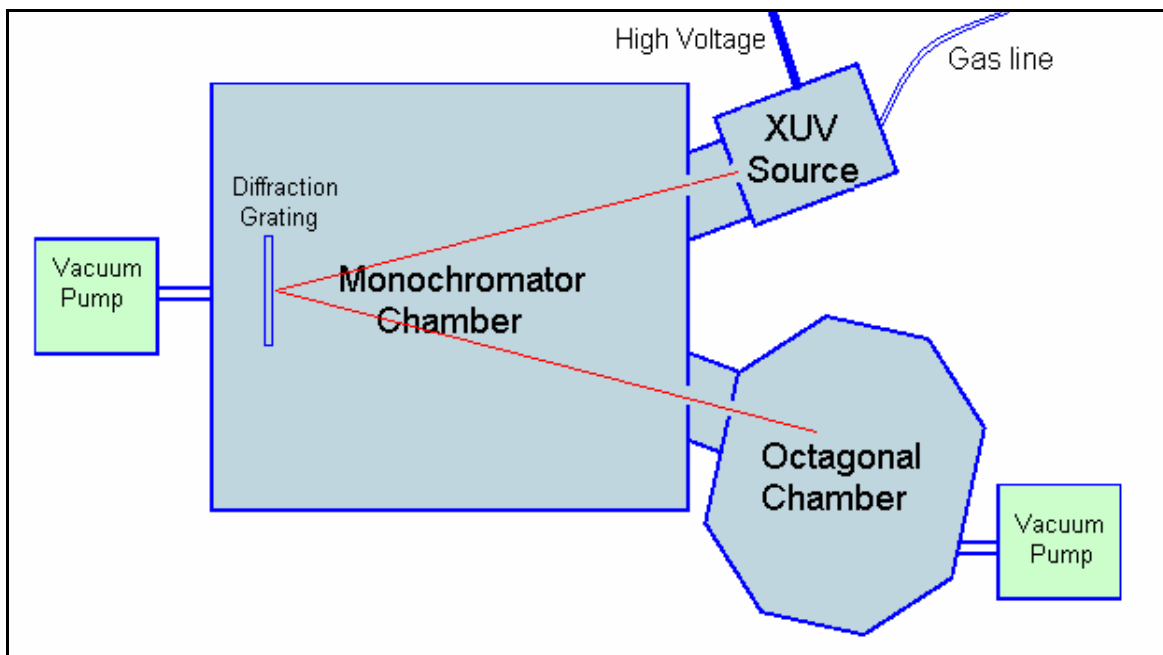


Figure A.1: Monochromator and reflectometer layout

The monochromator is used to select a narrow band of wavelengths for use in the reflectometer, or o-chamber (for its octagonal shape). The system must be kept under vacuum since EUV light is absorbed in only a few millimeters of air. Light is created in an appendage to the monochromator using helium, hydrogen, or neon gas ionized by a voltage source of 700kV DC (Figure A.2). The resulting plasma releases light in spectral

lines characteristic of gas used. Tables showing predominant peaks for different gases can be found on the NIST website [17]. The type of gas is changed depending on the wavelengths studied. A pinhole in the wall between the source and monochromator allows the light to pass into the monochromator while restricting gas flow. The light source must be differentially pumped in order to keep enough gas in the source for a stable light, while keeping the rest of the system under a low enough vacuum that the short wavelengths of interest are not absorbed.

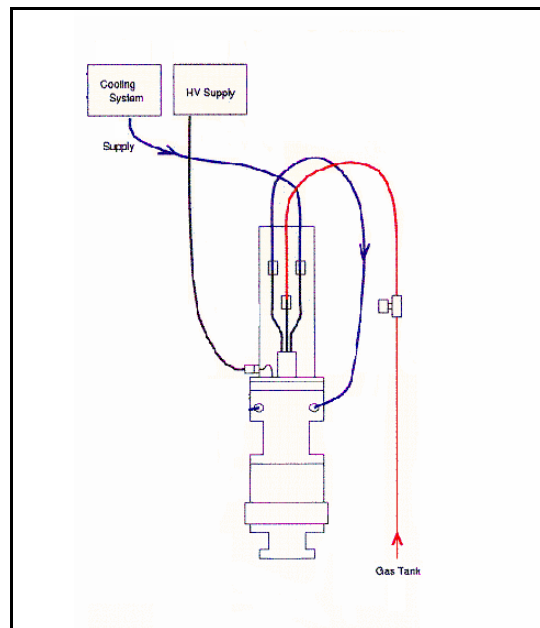


Figure A.2: Hollow cathode light source

The light entering the monochromator is incident on a diffraction grating that splits the light, reflecting different wavelengths at different angles, just as a prism refracts light into a rainbow. The desired wavelength is directed through the baffles leading to the o-chamber by turning the grating about a vertical axis through its center.

We have two gratings, one of 1200 lines per millimeter and the other of 600 lines per millimeter. The monochromator is calibrated for the grating of 600 lines/mm, so the wavelength read on the side of the monochromator is correct when that grating is used. When the other grating is in use, the actual wavelength is one half what is read.

Just beyond the baffles is a pinhole to collimate the beam. A smaller pinhole will make the beam more point-like so that all of the light passes directly over the center of the o-chamber, making the experiment accurate as far as placement of the beam. There is a trade off, however, when making the beam too small. Such a small pinhole would not allow the needed intensity of light through. A smaller amount of light for use in experimentation would lead to greater statistical inaccuracy.

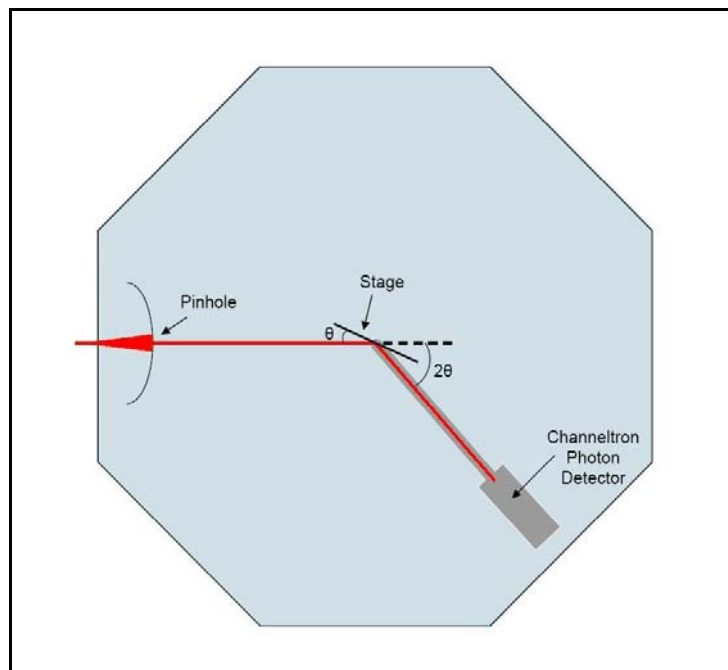


Figure A.3: Reflectometer schematic

The light passes from the pinhole over the center of the o-chamber and then, unless deflected, into the detector at the back of the chamber (Figure A.3). The film (also called a mirror or sample) of interest is located at the center of the chamber. The film is mounted on a stage that may be operated from the computer for movement while the system is under vacuum. The stage can be rotated for measurements or moved out of the beam for normalization of measurements. The detector is also controlled from the computer. It is generally placed at twice the angle of the stage so that the reflected beam is directed toward it.

All of the stages inside of the o-chamber can be run remotely using LabView programs. The most used programs are stagecontrolspring.vi, channeltron.vi, and VAR-Automated.vi or updated versions of them. Stagecontrol is used for moving individual stages a known distance. Channeltron allows the detector to be run, plots photon counts as read by the detector, and allows steady movement of stages in time as photon counts are being taken. These two programs are used in alignment and maintenance of the system. VAR is the program used for taking data. It produces plots of reflectance versus angle. This program is discussed in more detail in the improvements section.

A.2 Improvements

My first assignment with the monochromator was to find and fix a leak that was causing the base pressure on the outside of the entrance slit to be as high as 75 mtorr instead of the desired pressure of about 15 mtorr. Elke Jackson noticed that the plexiglas piece insulating the monochromator from the light source had a crack, so together we

milled a new one. The screw holes stripped as soon as we installed the new piece, so Wes Lifferth, the department machinist, made another from a bullet proof plastic.

The new piece didn't fix the leak, so I next used methyl alcohol in an attempt to find the leak. By sealing off a different piece each time the system was evacuated, the leak had been traced to the arm of the monochromator past the hollow cathode light source. I squirted this suspected part with methyl alcohol. If the leak was large enough, a jump in the pressure would be seen when the leak was sprayed and alcohol was sucked into the system. I first squirted large areas to narrow down the possible area where the leak could be. Having identified the tube from the He gas tank as the culprit, I sprayed each joint or valve one at a time, waiting for the alcohol to dry before spraying again so that if there were a jump in pressure I would know exactly where the leak was. The problem was discovered in the welding at the end of the suspected tube (Figure A.4). Wes Lifferth cut off the old end and welded a new one on. With the part replaced, the base pressure dropped to 12 mtorr.

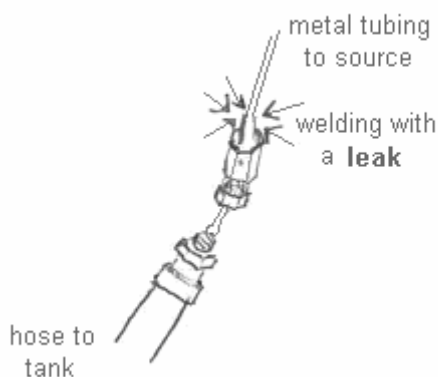


Figure A.4: Spot of leak in light source gas line

Shortly after I became involved with the monochromator, construction on the Eyring Science Center was finished and the system had to be moved. This meant that the entire system had to be disassembled and then put back together and realigned. Alignment is explained in the Initial Alignment SOP (See Appendix B). The next laborious task was to manually align the pinhole, which could only be done with the o-chamber at atmosphere, and then to check the alignment using the EUV light, which can only be done under vacuum. This must be done many times before the alignment is correct. To save future users from having to repeat this process several tens of times, stages that could be operated outside of the o-chamber via a controller box were ordered for the pinhole with much help from Jennie Guzman. This way the alignment can all be done under vacuum. When the stages arrived, they had been anodized (covered with a vacuum-incompatible coating) and so were not fit for use in our vacuum system because they would outgas. They had to be sent back for reconstruction without the coating. The stages have since been installed and the pinhole can now be aligned in under ten minutes.

Several improvements were made to the LabView program VAR-Automated.vi. This program is used to take data and make plots once all alignment is finished. The original program assumed that the alignment was perfect at the start of the program and that the mirror and detector motors stayed exactly in the desired configuration of $\theta/2\theta$ for all θ (see Figure A.3). Guzman and I updated the program so that it will make fine corrections to alignment. It is still necessary to align the detector to within 2 degrees and the mirror stages to within 1.5 degrees for theta and then set these positions as zero in stagecontrolspring.vi. The new VAR program will first move the mirror out of the beam and scan the detector from -2 to 2 degrees.

The result of the detector scan looked like a saddle point (Figure A.5). For consistency, the minimum in the center, or the saddle point, was determined to be the center. After the pinhole was moved, the detector scan from -2 to 2 degrees no longer showed a saddle point (Figure A.6), so it may be more accurate in the future to use a full-width-half-max approach. This would be done by finding the points on either side of the beam where the intensity is half of the maximum. The center of the beam is then assumed to be half way between to the points of half-maximum intensity and the detector is zeroed at that point. Rather than simply using the maximum as the center of the beam, this technique is less sensitive to noise.

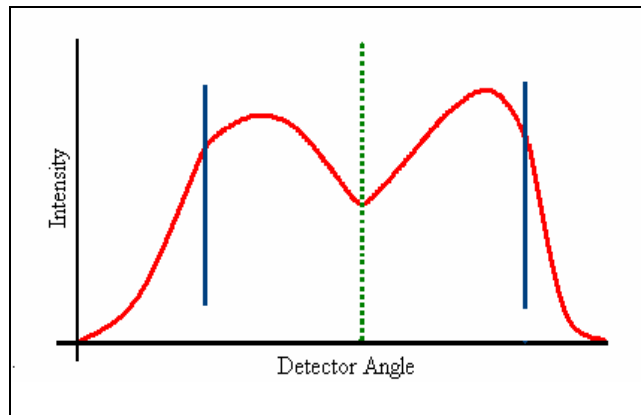


Figure A.5: Saddle point in beam profile

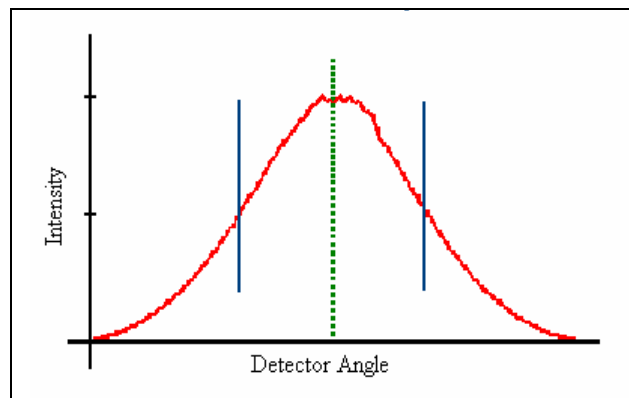


Figure A.6: Full-width half-max approach to finding beam center

After the center of the beam is found and the intensity is measured, the mirror is moved back into the beam. The VAR program aligns the mirror by moving it into the beam using the x-motor until the intensity reaching the detector is 60% of the original. This way the film is as close to the center for the beam as possible. The theta motor then moves counterclockwise 2 degrees, scans clockwise through 3 degrees, and is returned to the position that lets the greatest intensity reach the detector. This puts the mirror parallel to the beam. This process of moving the x- and theta-motors is repeated 3 times.

When we finally had been running the repaired monochromator to take measurements for less than a week, a virus went around BYU. Whether for this or another reason, the computer began sending sporadic messages to the stage motors without even having the VI's open. The National Instruments DAQ board had to be replaced. The stages rotated many times, twisting and braking wires, and ruining the drivers. Just before her summer REU was over, Guzman began circuit diagrams of the interlock box and other o-chamber circuitry that have since been finished. With help and direction from John Ellsworth and help from Niki Farnsworth, Liz Strein, and Jennie Guzman, the system has been rewired and is now much more robust. Many previous grounding problems were solved and buffers were installed to protect the drivers in case this ever happens again.

In December 2003 the channel electron multiplier (CEM) in the channeltron detector was replaced. The x-, y-, and z-direction motors were also replaced with new ones.

Appendix B
Standard Operating Procedures

Bibliography

- [1] D. D. Allred, M. B. Squires, R. S. Turley, W. Cash, and A. Shipley. "Highly reflective uranium mirrors for astrophysics applications," Proc. SPIE **4782**, 212-223 (2002).
- [2] S. Lunt, "Determining the indices of refraction of reactively sputtered uranium dioxide thin films from 46 to 584 angstroms," M.S. Thesis (Brigham Young University, Provo, UT, 2000).
- [3] <http://www.nanoword.net/library/weekly/aa102900a.htm>, February 6, 2004.
- [4] <http://public.itrs.net/Files/2003ITRS/Home2003.htm>, January 7, 2004.
- [5] K. Takemoto, et. al., "Transmission x-ray microscopy with 50 nm resolution in Ritsumeikan synchrotron radiation center," X-ray Microscopy AIP conference proceedings 446-51 (2-6 Aug 1999).
- [6] V.G. Kohn. "On the theory of reflectivity by an x-ray multilayer mirror," Phys. Stat. Sol. **185**(61), 61-70 (1995).
- [7] L.G. Parratt. "Surface studies of solids by total reflection of x-rays," Physical Review **95** (2), 359-369 (1954).
- [8] http://www-cxro.lbl.gov/optical_constants/mirror2.html, January 22, 2004.
- [9] E. Spiller, Soft X-ray Optics, (SPIE Optical Engineering Press, 1994), p.6-13.
- [10] J. D. Jackson, Classical Electrodynamics, 3rd ed. (John Wiley & Sons, Inc., New York, 1998), p. 310 and 330.
- [11] L. Black, F. Miserque, T. Gouder, L. Havela, J. Rebizant, and F. Watsin. "Preparation and photoelectron spectroscopy study of UN_x thin films," Journal of Alloys and Compounds **315**, 36-41 (2001).
- [12] <http://volta.byu.edu/adamson03.pdf>, November 11, 2003.
- [13] D. Windt, "IMD—software for modeling the optical properties of multilayer films," American Institute of Physics **12** (4), 360-370 (1998).
- [14] R.M. Dell, V.J. Wheeler, and N.J. Bridger. "Hydrolysis of uranium mononitride," Faraday Soc. Trans. **63**, 1286-94 (1967).
- [15] <http://www.weizmann.ac.il/surflab/peter/afmworks/>, November 4, 2003.

[16] <http://www.lbl.gov/>, September 8, 2003.

[17] <http://physics.nist.gov/PhysRefData/Handbook>, February 12, 2004.